Spherical Harmonic Mapping of Dyslexia

****

****

Abstract. Exploring differences in the brain surface is a paramount, yet challenging research area. We propose a new framework for constructing brain maps that can help to distinguish the surface differences across dyslexic and control brains. Using 3D volume registration and 3D Spherical Harmonic (SPHARM) alignment techniques, the framework sequentially (*i*) segments the 3D brain cortex; (*ii*) registers the segmented volume to a reference volume; (*iii*) constructs a 3D Delaunay triangulation mesh; (*iv*) decomposes the mesh with SPHARM and aligns the mesh to a reference, and (*v*) statistically analyze the mesh nodes on the brain surface. Our experimental results confirm that the framework is able to detect the goal surface differences and potentially improve understanding and clinical diagnostic information available to physicians.

Keywords: Brain mapping, Spherical Harmonics (SPHARM), shape analysis, dyslexia, brain cortex

1 INTRODUCTION

The neurological disorder of dyslexia is difficult to diagnose and has a profound impact on a child's ability to fluently read and comprehend words despite the fact that they possess a normal intelligence level for their age and education [1]. Dyslexia is not uncommon, as it affects roughly 5-12% of the population [2]. However, it is often diagnosed only after a child's scholastic performance or lifestyle has already been impacted.

According to multiple studies, structural differences are found in the brains of subjects with dyslexia. The earliest findings revealed a lack of the typical brain asymmetry and an increase in cortical anomalies [2]. According to Eliez et al. [3] and Casanova et al. [4], dyslexic subjects have smaller gyral indexes (the ratios between the pial contours and the convex hull of the brain surface) than normal subjects, suggesting that the dyslexic brains differ in folding. The recent comprehensive reviews by Richlan et al. [5] and Krafnick et al. [6] have demonstrated evidence of change in the bilateral temporoparietal and left occipitotemporal cortical regions of the brain's gray matter. Using voxel-based morphometry to examine in-vivo dyslexic brains, Eliez et al. [3] and Silani et al. [7] have indicated reduced gray matter volume in such brains. Klingberg et al. [8] and Niogi et al. [9] also examined the cerebral white matter by using diffusion tensor imaging and found similar results. By analyzing MRIs, Elnakib et al. [10] and von Plessen et al. [11] discovered significant differences in the shapes

and body length of the corpus callosum in key anatomical regions that help to identify dyslexia.

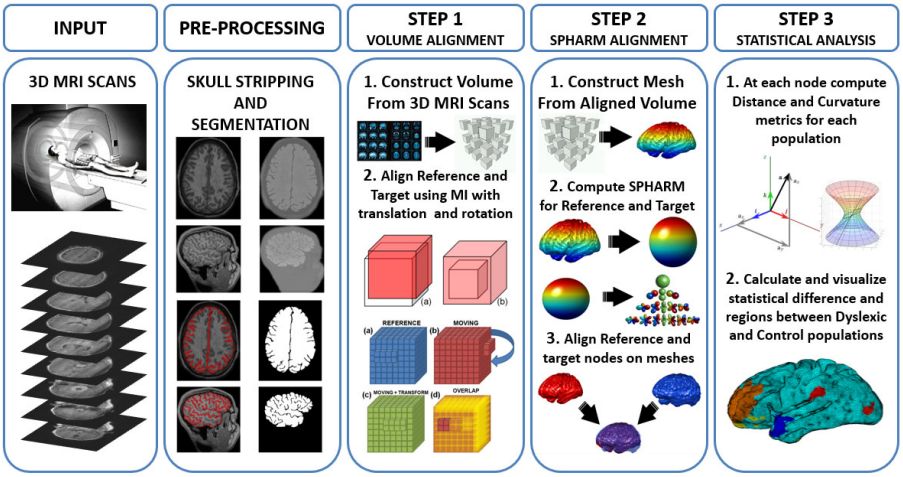

Fig. 1. Block diagram of the proposed brain mapping framework: the brain MRI scans are first segmented and then co-aligned using a mutual information (MI) based rigid 3D volume registration, followed by mesh construction and surface registration using Spherical Harmonics (SPHARM) decomposition; then statistical differences between populations of the mesh nodes are examined using distance and curvature metrics.

We focus on the cerebral cortex of the brain and propose a new framework for mapping the brain in order to explore differences of the dyslexic brains. Our framework (Fig. 1) performs the following image processing steps: (*i*) 3D brain cortex segmentation; (*ii*) registration of the segmented 3D volume to a reference atlas volume; (*iii*) construction of a 3D Delaunay triangulation mesh; (*iv*) 3D Spherical Harmonics (SPHARM) decomposition and registration of the mesh, and (*v*) statistical analysis of individual mesh nodes across the brain's surface.

2 3D BRAIN SURFACE ANALYSIS STEPS

2.1 Brain Cortex Segmentation

Accurate cortex segmentation from 3D T1-MRI scans is a challenging problem because of similar pixel-wise image intensities in both the cortex and the surrounding organs. As a solution, we use our previously introduced parametric deformable 3D boundary evolution [12], which is controlled with three probabilistic models, namely, a first-order visual appearance, a learned shape prior, and a spatial second-order model of the volume to be segmented (see [12] for more detail).

2.2 3D Volume Registration

In order to accurately examine the brain surface, the target brain volumes are aligned to a reference volume using geometric transformations (rigid Euclidean

movements) selected by unconstrained optimization of a nonlinear fitness function. The latter combines two weighed terms depending on relative (x, y, z)-translations and rotations (denoted below $\boldsymbol{\theta}$) of a target 3D volume with respect to a reference. Scaling and shearing, which result in erroneous brain shape distortions, are excluded from the transformations.

The fitness terms evaluate the alignment by the relative 3D mutual information (MI) and voxel overlap between the volumes. The MI (see, e.g., [13]) is computed between distance maps for the reference and target volumes, each map being formed by the Multi-Stencils Fast Marching Method [14]. The relative 3D MI is as follows:

$$E_{\mathrm{mi}}(\boldsymbol{\theta}) = \frac{M_{\mathrm{tar}}(\boldsymbol{\theta})}{M_{\max}} \tag{1}$$

where $M_{\mathrm{tar}}(\boldsymbol{\theta})$ and $M_{\max}$ are the MI between the transformed target and reference, and the maximal MI between the reference and itself, respectively.

The relative voxel overlap is calculated as

$$E_{\mathrm{voxel}}(\boldsymbol{\theta}) = 1 - \frac{\sum_{(i,j,k)=(1,1,1)}^{(I,J,K)} |V_{\mathrm{tar}}(i,j,k;\boldsymbol{\theta}) - V_{\mathrm{ref}}(i,j,k)|}{\sum_{(i,j,k)=(1,1,1)}^{(I,J,K)} V_{\mathrm{ref}}(i,j,k)} \tag{2}$$

where $V_{\mathrm{ref}}(i,j,k)$ and $V_{\mathrm{tar}}(i,j,k;\boldsymbol{\theta})$ denote binary voxel values indicating the presence (1) or absence (0) of the reference and transformed target volumes, respectively, within their common 3D voxel space of the size $I \times J \times K$. The weighted fitness function $F_{\mathrm{fit}}(\boldsymbol{\theta})$ to be maximized is then:

$$F_{\mathrm{fit}}(\boldsymbol{\theta}) = w_{\mathrm{mi}} E_{\mathrm{mi}}(\boldsymbol{\theta}) + w_{\mathrm{voxel}} E_{\mathrm{voxel}}(\boldsymbol{\theta}) \tag{3}$$

where w_{mi} and w_{mi} are pre-selected fixed weights (in our experiments, $w_{\mathrm{mi}} = w_{\mathrm{mi}} = 0.5$ assuming equal contributions of both the terms).

The unconstrained nonlinear maximization of this function searches for the translations and rotations, $\boldsymbol{\theta}^* = \arg\max_{\boldsymbol{\theta}} F_{\mathrm{fit}}(\boldsymbol{\theta})$, of a target volume, aligning it closely to the reference volume. An iterative block-coordinate descent optimization was used to circumvent the complicated and time-consuming simultaneous optimization of the six translation-rotation parameters. The block-coordinate optimization toggles between the translation and rotation, repeating the cycles until convergence, i.e. no further changes of the parameters $\boldsymbol{\theta}^*$ are found.

2.3 Spherical Harmonics (SPHARM) Shape Analysis

Using SPHARM representations greatly simplifies surface registration in comparison to locating point-to-point correspondences, where correspondences are established manually or can be found analytically. The spectral SPHARM analysis [15, 16] considers a 3D surface as a linear combination of specific basis functions. To perform a SPHARM based comparison, a surface manifold of the brain cortex for both the reference and target volumes is approximated with a triangulated 3D Delaunay mesh [17] consisting of 50,000 individual nodes to ensure

high surface accuracy. Unit spheres for each manifold are constructed by organizing the mesh nodes in line with two properties of the "*Attraction-Repulsion*" mapping [18]: (*i*) the unit distance of each node from the brain cortex center and (*ii*) the equal distances of each node from its nearest neighbors.

Let Ω denote a pair of polar and azimuthal spherical angles related to a 3D point on the cortical surface supported by the unit sphere. The target, T, and reference, R, meshes consist each of n nodes: $T = \{\mathbf{t}(\Omega_i) : i = 1, \ldots, n\}$ and $R = \{\mathbf{r}(\Omega'_i) : i = 1, \ldots, n\}$, where $\mathbf{t}\,(\Omega_i) = [x_{\rm t}(\Omega_i), y_{\rm t}(\Omega_i), z_{\rm t}](\Omega_i)]$ and $\mathbf{r}\,(\Omega'_i) = [x_{\rm r}(\Omega'_i), y_{\rm r}(\Omega'_i), z_{\rm r}](\Omega'_i)]$ denote the 3D (x, y, z)-coordinates of the mesh nodes. These target and reference nodes relate to their own, and generally unrelated, spherical angles $\{\Omega_i : i = 1, \ldots, n\}$ and $\{\Omega'_i : i = 1, \ldots, n\}$, respectively.

The SPHARMs, $Y_{lm}(\Omega)$, of degree l; $l = 0, 1, \ldots, k$, and order m; $-l \leq m \leq l$, form a set of the orthonormal functions on the sphere [15]. The orthonormality holds with respect to the inner product, $\langle f, \varphi \rangle$, of the arbitrary functions, $f(\Omega)$ and $\varphi(\Omega)$, supported by the sphere.

Weighted k-degree SPHARM approximations, $T_{\rm ap}$ and $R_{\rm ap}$, of the target and reference surfaces, respectively are defined as follows [20]:

$$\mathbf{t}_{\rm ap}(\Omega) = \sum_{l=0}^{k} \sum_{m=-l}^{l} w_l \mathbf{b}_{lm} Y_{lm}(\Omega);\ \mathbf{r}_{\rm ap}(\Omega) = \sum_{l=0}^{k} \sum_{m=-l}^{l} w_l \mathbf{b}'_{lm} Y_{lm}(\Omega) \qquad (4)$$

where a smoothing degree-dependent weight, $w_l = e^{(-l(l+1)\sigma)}$; $\sigma > 0$, is selected empirically to reduce Gibbs ringing artifacts in these approximate surfaces and the vectorial SPHARM coefficients, $\mathbf{b}_{lm} = [\langle x_{\rm t}, Y_{lm} \rangle, \langle y_{\rm t}, Y_{lm} \rangle, \langle z_{\rm t}, Y_{lm} \rangle]$ and $\mathbf{b}'_{lm} = [\langle x'_{\rm t}, Y_{lm} \rangle, \langle y'_{\rm t}, Y_{lm} \rangle, \langle z'_{\rm t}, Y_{lm} \rangle]$ are computed on the basis of the target, T, and reference, R, mesh nodes and SPHARM functions $Y_{lm}(\Omega)$.

The approximations of Eq. (4) map the target surface to the reference mesh, which can be used for exploring sulcal and gyral folding patterns [19]. The mapping preserves the target shape and curvature and relates them to the reference nodes by interpolating, if necessary, between the neighboring mapped target nodes.

2.4 Statistical Metrics for Brain Mapping

Each node of the target mesh following the 3D volume and SPHARM registration is characterized with four statistical metrics, namely, the Euclidean distance from the origin and the Gaussian, mean, and normal surface curvatures [21]. Statistical node-wise p-values between the brain meshes for the control and dyslexic populations are computed using an unpaired t-test at the 95% significance level.

3 Experimental Results

The proposed framework has been examined using *in-vivo* data collected from 30 age-matched subjects (16 dyslexic and 14 control ones of age from 18 to 40

years in each group). The subjects were scanned with a 1.5 Tesla GE MRI system with voxel resolution of $0.9375 \times 0.9375 \times 1.5\ mm^3$ under a T1-weighted imaging sequence protocol. The reference brain was constructed from the Montreal Neurological Institute's ICBM 152 atlas [22, 23]. All results are displayed as overlays on the reference brain.

Fig. 2 displays the p-values at each node, which highlight detected areas of significant differences on the brain surface between the dyslexic and control populations as quantified using our proposed framework. The brighter the nodal color, the more statistically significant the node. For better clarity, nodes below the statistical significance threshold are indicated using a uniform background color.

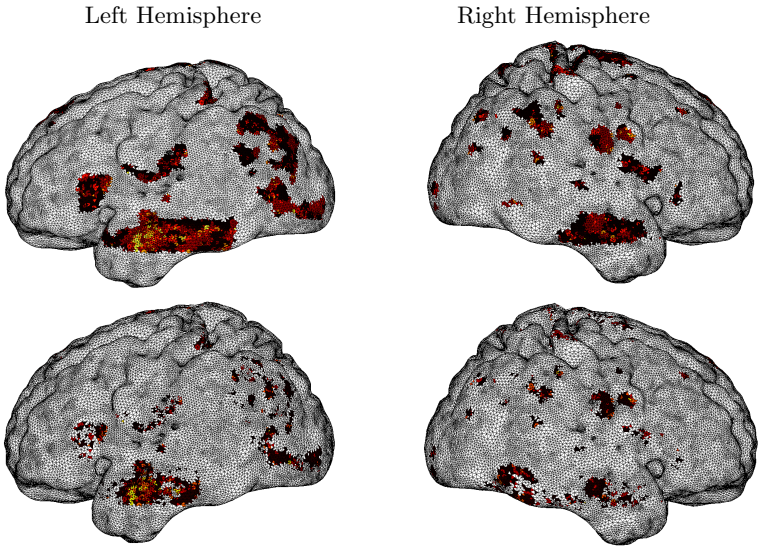

Fig. 2. Brain nodes with statistically significant differences ($p < 0.05$) in the measured distance **or** curvature (top), and nodes significant differences in **both** the distance **and** curvature (bottom). Insignificant nodes are white; otherwise the brighter the color, the more significant the node (i.e. the darkest nodes have the least significance.

By visual comparisons, our results confirm other known brain studies, e.g., by Richlan et al. [5, 24], Krafnick et al. [6], and Talan et al. [25], who have highlighted key brain areas widely recognized as related to phonological processing and dyslexia. Figure 3 overlays some of these key areas onto our brain map of significant differences in order to demonstrate that the significant areas indicated by the proposed framework include the key areas found in the aforementioned studies. Our results on an independent data set provide clear evidence that supports Richlan and Krafnick's recommendations for identifying specific locations of the most prominent differences between the dyslexic and control subjects.

The brain cortex is typically divided into four lobes: frontal, parietal, occipital, and temporal. To make the measurements more detailed, the frontal lobe can be subdivided into the prefrontal and premotor areas. As shown in Table 1,

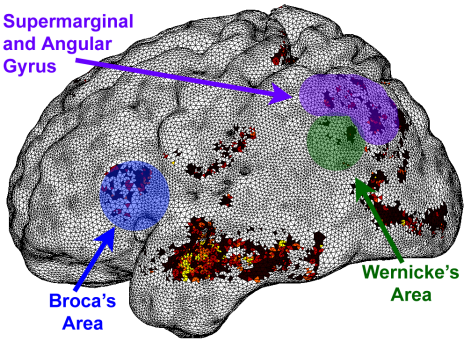

Fig. 3. The uniquely colored Broca's and Wernicke's areas, as well as the supermarginal and angular gyrus on the left brain hemisphere together with areas of significant difference in both distance and curvature measurements. Significantly different nodes are found in brain areas that correlate with phonological processing.

the absolute numbers of the significantly different nodes or their relative numbers (percentages of the total brain nodes) can easily be counted for each of these five brain areas. That the temporal and parietal lobes contain major areas of difference comes quite expectably because the key areas associated with language processing reside in these brain lobes. Nonetheless, the proposed mapping provides potentially useful quantitative characteristics and more precise locations of the areas of the key dyslexic-to-normal brain differences. Furthermore the approach has discovered significantly different areas that neighbor these key primary phonological processing areas. A potential reason for the occurence of these differences may be related to migrations in brain function, where alternate parts of the brain work help to compensate in dyslexic individuals, a new theory proposed by Talan et al. [25].

	Left Hemisphere		**Right Hemisphere**	
Brain Region	N_{sd}	ν_{sd},%	N_{sd}	ν_{sd},%
Prefrontal	0	0	0	0
Premotor	309	0.6	547	1.1
Parietal	939	1.8	1073	2.1
Occipital	706	1.4	185	0.3
Temporal	734	1.4	478	0.9
Totals	**2688**	**5.3**	**2283**	**4.5**

Table 1. Numbers N_{sd} and relative numbers ν_{sd} (% of the total nodes) of the significantly different nodes in the primary prefrontal, premotor, parietal, occipital, and temporal brain regions.

4 DISCUSSION AND CONCLUSION

This novel framework examines statistical differences across the surface of brains between dyslexic and control populations. Combining a volumetric registration with a SPHARM alignment enables detailed comparison of individual positions

on the surface of the brain. Parameters, such as distance and curvature, indicate that there are differences between dyslexic and control subjects. The results of our research indicate differences in areas of the brain that correspond to predictions by Richlan et al. [5, 24] and Krafnick et al [6]. While differences were detected in expected brain regions, the approach located additional differences in neighboring and alternative brain regions. These findings warrant further examination and there are plans to continue and expand this work for neurological disorders, include mapping individual brain structures, to help isolate key differences useful for understanding the development of the human brain. The proposed brain mapping framework demonstrates promise for understanding and potentially improving diagnostic clinical information available to physicians.

References

1. K. R. Pugh, W. E. Mencl, *et al.*, "Functional neuroimaging studies of reading and reading disability(developmental dyslexia)," *Mental Retardation and Developmental Disabilities Research Reviews*, vol. 6, no. 3, pp. 207–213, 2000.
2. G. Lyon, S. Shaywitz, *et al.*, "A definition of dyslexia," *Annals of Dyslexia*, vol. 53, no. 1, pp. 1–14, 2003.
3. S. Eliez, J. M. Rumsey, *et al.*, "Morphological alteration of temporal lobe gray matter in dyslexia: an MRI study," *Journal of Child Psychology and Psychiatry*, vol. 41, no. 5, pp. 637–644, 2000.
4. M. F. Casanova, J. Araque, *et al.*, "Reduced brain size and gyrification in the brains of dyslexic patients," *Journal of Child Neurology*, vol. 19, no. 4, pp. 275–281, 2004.
5. F. Richlan, M. Kronbichler, *et al.*, "Structural abnormalities in the dyslexic brain: A meta-analysis of voxel-based morphometry studies," *Human Brain Mapping*, vol. 34, no. 11, pp. 3055–3065, 2013.
6. A. J. Krafnick, D. L. Flowers, *et al.*, "An investigation into the origin of anatomical differences in dyslexia," *The Journal of Neuroscience*, vol. 34, no. 3, pp. 901–908, 2014.
7. G. Silani, U. Frith, *et al.*, "Brain abnormalities underlying altered activation in dyslexia: a voxel based morphometry study," *Brain*, vol. 128, no. 10, pp. 2453–2461, 2005.
8. T. Klingberg, M. Hedehus, *et al.*, "Microstructure of temporo-parietal white matter as a basis for reading ability: evidence from diffusion tensor magnetic resonance imaging," *Neuron*, vol. 25, no. 2, pp. 493–500, 2000.
9. S. N. Niogi and B. D. McCandliss, "Left lateralized white matter microstructure accounts for individual differences in reading ability and disability," *Neuropsychologia*, vol. 44, no. 11, pp. 2178–2188, 2006.
10. A. Elnakib, A. El-Baz, *et al.*, "Image-based detection of corpus callosum variability for more accurate discrimination between dyslexic and normal brains," in *2010 IEEE International Symposium on Biomedical Imaging: From Nano to Macro (ISBI'10)*. IEEE, 2010, pp. 109–112.
11. K. von Plessen, A. Lundervold, *et al.*, "Less developed corpus callosum in dyslexic subjectsa structural MRI study," *Neuropsychologia*, vol. 40, no. 7, pp. 1035–1044, 2002.
12. Anonymous
13. C. E. Shannon, "A mathematical theory of communication," *ACM SIGMOBILE Mobile Computing and Communications Review*, vol. 5, no. 1, pp. 3–55, 2001.

14. M. S. Hassouna and A. A. Farag, "Multistencils fast marching methods: A highly accurate solution to the eikonal equation on cartesian domains," *IEEE Transactions on Pattern Analysis and Machine Intelligence*, vol. 29, no. 9, pp. 1563–1574, 2007.
15. G. Gerig, M. Styner, *et al.*, "Shape analysis of brain ventricles using spharm," in *IEEE Workshop on Mathematical Methods in Biomedical Image Analysis (MMBIA 2001)*. IEEE, 2001, pp. 171–178.
16. M. K. Chung, K. M. Dalton, *et al.*, "Weighted fourier series representation and its application to quantifying the amount of gray matter," *IEEE Transactions on Medical Imaging*, vol. 26, no. 4, pp. 566–581, 2007.
17. Q. Fang and D. A. Boas, "Tetrahedral mesh generation from volumetric binary and grayscale images," in *IEEE International Symposium on Biomedical Imaging: From Nano to Macro (ISBI'09)*. IEEE, 2009, pp. 1142–1145.
18. Anonymous
19. M. K. Chung, R. Hartley, *et al.*, "Encoding cortical surface by spherical harmonics," *Statistica Sinica*, vol. 18, no. 4, p. 1269, 2008.
20. M. K. Chung, K. M. Dalton, *et al.*, "Tensor-based cortical surface morphometry via weighted spherical harmonic representation," *IEEE Transactions on Medical Imaging*, vol. 27, no. 8, pp. 1143–1151, 2008.
21. E. Abbena, S. Salamon, *et al.*, *Modern Differential Geometry of Curves and Surfaces with Mathematica*. CRC press, 2006.
22. V. S. Fonov, A. C. Evans, *et al.*, "Unbiased average age-appropriate atlases for pediatric studies," *NeuroImage*, vol. 54, no. 1, pp. 313–327, 2011.
23. ——, "Unbiased nonlinear average age-appropriate brain templates from birth to adulthood," *NeuroImage*, vol. 47, p. S102, 2009.
24. F. Richlan, M. Kronbichler, *et al.*, "Functional abnormalities in the dyslexic brain: A quantitative meta-analysis of neuroimaging studies," *Human Brain Mapping*, vol. 30, no. 10, pp. 3299–3308, 2009.
25. J. Talan, "A new theory and brain areas implicated to explain dyslexia," *Neurology Today*, vol. 14, no. 3, pp. 12–13, 2014.